CrossMark

# Origin of Galactic Spurs: New Insight from Radio/X-Ray All-sky Maps

Jun Kataoka[1] , Marino Yamamoto[1], Yuki Nakamura[1], Soichiro Ito[1], Yoshiaki Sofue[2] , Yoshiyuki Inoue[3,4,5] ,
Takeshi Nakamori[6], and Tomonori Totani[7]

[1] Faculty of Science and Engineering, Waseda University, 3-4-1, Okubo, Shinjuku, Tokyo 169-8555, Japan; kataoka.jun@waseda.jp
[2] Institute of Astronomy, The University of Tokyo, 2-21-2, Osawa, Mitaka-shi, Tokyo 181-0015, Japan
[3] Department of Earth and Space Science, Osaka University, 1-1 Machikaneyamacho, Toyonaka, Osaka, 560-0043, Japan
[4] Interdisciplinary Theoretical & Mathematical Science Program (iTHEMS), RIKEN, 2-1 Hirosawa, Saitama 351-0198, Japan
[5] Kavli Institute for the Physics and Mathematics of the Universe (WPI), UTIAS, The University of Tokyo, Kashiwa, Chiba 277-8583, Japan
[6] Department of Physics, Faculty of Science, Yamagata University, 990-8560, Japan
[7] Department of Astronomy, The University of Tokyo, 7-3-1, Hongo, Bunkyo-ku, Tokyo 113-0033, Japan

## Abstract

In this study, we analyze giant Galactic spurs seen in both radio and X-ray all-sky maps to reveal their origins. We discuss two types of giant spurs: one is the brightest diffuse emission near the map's center, which is likely to be related to Fermi bubbles (NPSs/SPSs, north/south polar spurs, respectively), and the other is weaker spurs that coincide positionally with local spiral arms in our Galaxy (LAS, Local Arm spur). Our analysis finds that the X-ray emissions, not only from the NPS but also from the SPS, are closer to the Galactic center by $\sim 5°$ compared with the corresponding radio emission. Furthermore, larger offsets of $10°$–$20°$ are observed in the LASs; however, they are attributed to different physical origins. Moreover, the temperature of the X-ray emission is $kT \simeq 0.2$ keV for the LAS, which is systematically lower than those of the NPS and SPS ($kT \simeq 0.3$ keV) but consistent with the typical temperature of Galactic halo gas. We argue that the radio/X-ray offset and the slightly higher temperature of the NPS/SPS X-ray gas are due to the shock compression/heating of halo gas during a significant Galactic explosion in the past, whereas the enhanced X-ray emission from the LAS may be due to the weak condensation of halo gas in the arm potential or star formation activity without shock heating.

## 1. Introduction

The all-sky survey is a unique, albeit the only, approach for revealing giant structures in the sky that are rarely seen in pointing observations with a limited field of view (FOV). Haslam et al. (1982) conducted the first complete radio survey, which was measured at 408 Hz; the survey confirmed various giant spurs and loop structures extending over the entire sky. Of particular note was Loop I, a continuum loop spanning across $100°$ in the sky, and its brightest arm, known as the North Polar Spur (NPS). Initially, it was argued that NPS/Loop I was an old supernova remnant (SNR) that was extremely close to the Sun (Berkhuijsen et al. 1971); however, an alternative idea was proposed, suggesting that it was the remnants of starburst or nuclear outbursts in the Galactic center (GC) that occurred over 10 million years ago (Sofue 1977). Although the latter idea successfully explained similar structures observed in the south (South Polar Spur (SPS); Sofue 2000), it was almost neglected; however, it received renewed attention after the discovery of Fermi bubbles (Su et al. 2010).

Fermi bubbles are giant structures extending approximately $50°$ (or 8.5 kpc) above and below the GC, with a longitudinal width of $40°$. Notably, the NPS/Loop I exhibited close contact with Fermi bubbles. Moreover, Fermi bubbles are spatially correlated with the WMAP haze (Dobler & Finkbeiner 2008) measured between 20 and 50 GHz, which was confirmed later via Planck observations (Planck Collaboration et al. 2013). The connection between the NPS/Loop I and Fermi bubbles was widely discussed based on ROSAT all-sky X-ray maps (Snowden et al. 1995), although a positional offset between

radio and X-ray spurs was suggested (Sofue 2015; Kataoka et al. 2018). Using multiple observations with Suzaku, the X-ray emission from the NPS/Loop I was well represented by $kT \simeq 0.3$ keV thin thermal plasma (Kataoka et al. 2013); this may be interpreted as a result of shock heating of Galactic halo gas during the explosion, characterized initially by a temperature of $kT \simeq 0.2$ keV (Yoshino et al. 2008; Henley et al. 2010; Henley & Shelton 2013; Nakashima et al. 2018). More recently, eROSITA on the Spectrum–Roentgen–Gamma mission (Predehl et al. 2020a) launched in 2019 June provided a new, sharp all-sky map, in which a clear X-ray envelope surrounding Fermi bubbles was observed in both the northern and southern skies (Predehl et al. 2020b). Hence, the NPS/Loop I and SPS can now be regarded as the remnant of a Galactic explosion over 10 million years ago.

In addition to the above-mentioned giant structures, which are likely located in the GC, weaker but evident spurs were observed in all-sky radio maps. In fact, nonthermal spiral-arm emission along the Galactic plane is closely associated with the discrete spiral pattern of the Galaxy (Mills 1959; Sofue 1976; see also Nakanishi & Sofue (2006) for H I and $H_2$ patterns). Moreover, diffuse radio emissions emanating vertically from the Galactic plane are noteworthy; they are the most conspicuous at longitudes of $l \sim 80°$ and $\sim 260°$, i.e., exactly at the position of the Orion–Cygnus arms (or Local Arm), where our Sun is located. It has been argued that radio emissions associated with Local Arm spurs (LASs) are enhanced in nonthermal banks, which extend vertically up to $z \sim 1$ kpc from the Galactic plane (Sofue 1973, 1976, 2000). In this model, nonthermal banks are generated by inflations of magnetic fields with cosmic rays as a result of the Parker

instability (Parker 1966, 1969); hence, the inflation enhanced above gaseous spiral arms associated with Galactic shocked regions (Fujimoto 1968; Roberts 1969). In X-rays, similar diffuse emissions associated with LASs are visible in both ROSAT and eROSITA all-sky maps; however, their characteristics are yet to be elucidated. In this context, diffuse X-ray emission along spiral arms, whose morphology matched well with those in the mid-infrared or H$\alpha$ region, was discovered in nearby spiral galaxies by recent Chandra observations (Tyler et al. 2004; Long et al. 2014).

Herein we provide systematic comparisons of giant Galactic spurs observed in radio and X-ray all-sky maps to reveal their origins. The remainder of this paper is organized as follows. In Section 2, we present the method and result of correlation analysis to quantitatively discuss the positional offset between the radio and X-ray maps for all Galactic spurs. Next, we analyze the archival Suzaku data to reveal the origin of thermal X-ray emission associated with SPS and LAS regions; subsequently, we compare the results with those reported in the NPS/Loop I (Kataoka et al. 2013, 2018). In Section 3, we discuss the different characteristics of thermal emission in the NPS/SPS and LAS. We first discuss the origin of the comparable thickness and offset between the NPS and SPS; subsequently, we consider the origin of radio and X-ray emissions associated with LASs. Finally, a brief summary and future prospects are presented in Section 4.

## 2. Analysis and Results

### 2.1. Correlation Analysis of Radio and X-Ray All-sky Maps

We first compare the radio sky map obtained at 408 MHz (Haslam et al. 1982; contour) and the X-ray map measured at 0.75 keV based on the ROSAT all-sky survey (Snowden et al. 1995; color), as shown in Figure 1. The Galactic spurs analyzed herein are colored yellow, with the projection example for each rectangular region shown separately in the top panels. A significant offset was observed between the radio and X-ray profiles, at least for a certain fixed latitude $b$, as shown in Figure 1. Subsequently, we created a complete list of the radio/X-ray pixel values at the same Galactic position, $(l, b)$, with a 1° resolution in both the longitude and latitude directions. Next, we defined the source extraction region corresponding to the NPS, SPS, LAS1, and LAS2, as summarized in Table 1. Figure 2 shows the close-up view of the radio/X-ray maps for each region.

To be more precise, we first calculated the correlation coefficients $\rho$ between all radio and X-ray pixel values, i.e., $R(l, b)$ and $X(l, b)$, for each spur region. We defined $\rho[0]$ for raw radio and X-ray data as follows:

$$\rho[0] = \frac{\text{cov}(R, X)}{\sigma_R \, \sigma_X}, \qquad (1)$$

where cov$(R, X)$ is the covariance; $\sigma_R$ and $\sigma_X$ are the standard deviations of variables $R$ and $X$, respectively. Next, we calculated $\rho[\theta]$, which is the correlation coefficient between $R$ $(l+\theta, b)$ and $X(l, b)$, wherein the radio data were shifted by $\theta$ [°] in the longitude direction. In this context, a "positive" offset is defined as the direction to which the data are shifted toward the center of the Galactic east region ($0° < l < 180°$), and toward the anti-GC for the west region ($180° < l < 360°$).

The left panel of Figure 3 shows $\rho[\theta]$ as a function of $\theta$ for the NPS, SPS, LAS1, and LAS2, separately. It is noteworthy

that correlations were stronger for the NPS and SPS than for LAS1 and LAS2. Although we did not exclude point sources from all-sky X-ray maps, no such strong sources existed that affected the results of the correlation analysis presented herein. The amount of peak offset is summarized in the right panel of Figure 3 against Galactic longitude $l$. The errors in $\theta$ were estimated by approximating $\rho[\theta]$ using a single Gaussian function around the peak; hence, the uncertainties of peak positions were estimated in the right panel of Figure 3. The positional offsets between the radio and X-rays were $\theta = 6°.31 \pm 0°.34$ for the NPS and $\theta = -4°.17 \pm 0°.83$ for the SPS. Meanwhile, the offsets of the LASs were significantly larger, i.e., $\theta = 19°.35 \pm 0°.17$ for LAS1 and $\theta = -10°.57 \pm 0°.21$ for LAS2, respectively. We conclude that in all spurs the X-ray emission is shifted toward the GC direction compared with the corresponding radio emission by $5°$–$20°$.

It is noteworthy that the observed X-ray all-sky map is generally modified by absorption owing to the interstellar medium (mostly H I gas), particularly in the low-latitude regions within or near the Galactic disk and bulge. The amount of absorption depended on the distance to the structure of interest, which is, however, unknown for the NPS, SPS, and LASs analyzed in this study. Hence, we did not consider such modifications for the correlation analysis in this section. For this reason, we constrained the analysis regions to a relatively high Galactic latitude of $|b| > 15°$ (see Table 1), where the absorption was almost negligible.

### 2.2. Thermal Emission from SPS and LAS

The X-ray emission properties of the NPS/Loop I have been summarized and discussed in our previous papers (Kataoka et al. 2018 and references therein). Similarly, in this study we first investigated all the archival Suzaku data whose pointings were situated in the SPS, LAS1, and LAS2 regions, as listed in Table 2. We excluded pointings that contained either bright X-ray sources or extended sources such as Galaxy clusters, whose tailed emission might affect the analysis in the same FOV. Consequently, we discovered that four, five, and two pointings were used in the SPS, LAS1, and LAS2 regions, respectively. The pointing centers of the Suzaku observations and exposure in kiloseconds are listed in Table 2. The analysis procedure used was the same as those provided in the literature; hence, the results of Suzaku observations in the NPS regions (six points in the region defined in Table 1) were reproduced from the data by Kataoka et al. (2013).

In summary, we extracted the XIS data from XIS 0, 1, and 3, where XIS 0 and 3 were front-illuminated CCDs (FI-CCDs) and XIS 1 was a back-illuminated CCD (BI-CCD) that possessed better sensitivity than FI-CCDs below 1 keV but was less sensitive above 5 keV. We analyzed the Suzaku data using HEADAS software version 6.22, XSPEC version 12.9, and a calibration database released in 2016 April. We applied *sisclean* to remove hot and/or flickering pixels. Only data with a cutoff rigidity larger than 6 GV and day and night Earth data with an elevation angle larger than 20° were used for the analysis. We extracted the spectrum after removing possible point sources within the same FOV and then generated redistribution matrix files and auxiliary response files using *xisrmfgen* and *xissimarfgen* (Ishisaki et al. 2007). The non-X-ray background spectra from the night Earth observations were generated with *xisnxbgen*.
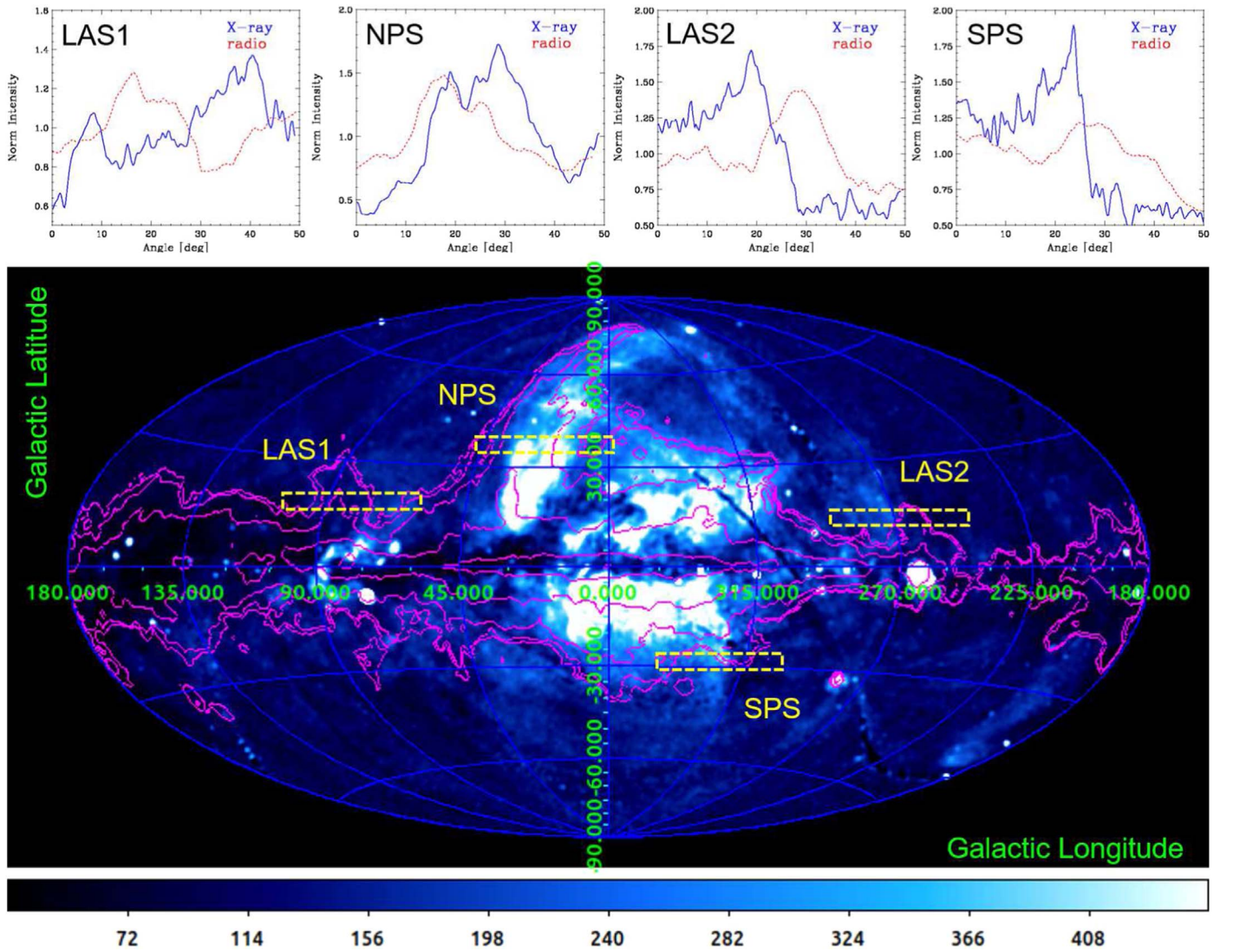
**Figure 1.** Galactic spurs analyzed in this paper. NPS: North Polar Spur; SPS: South Polar Spur; LAS1: Local Arm spur at $l \sim 80°$; LAS2: Local Arm spur at $l \sim 260°$. X-ray: 0.75 keV ROSAT all-sky map is shown in logarithmic color in units of $10^{-6}$ counts s$^{-1}$ arcmin$^{-2}$. Radio: 408 MHz all-sky map is shown as six-level contours (magenta) from 30 [K] to 600 [K] in logarithmic scale. Projections of radio/X-ray images along the Galactic longitude for each rectangular regions (yellow: approximately $50° \times 5°$ in longitude and latitude directions) are shown in the top panels, where intensities are normalized with each mean value.

**Table 1**
Regions for Correlation Analysis

| Source Region | Galactic Longitude | Galactic Latitude |
|---|---|---|
| NPS | $10° \leqslant l \leqslant 40°$ | $15° \leqslant b \leqslant 80°$ |
| SPS | $295° \leqslant l \leqslant 335°$ | $-60° \leqslant b \leqslant -15°$ |
| LAS1 | $60° \leqslant l \leqslant 95°$ | $15° \leqslant b \leqslant 35°$ |
| LAS2 | $240° \leqslant l \leqslant 280°$ | $15° \leqslant b \leqslant 35°$ |

For the spectral analysis, we used the $0.5-7.0$ keV data for XIS 0 and 3 and $0.4-5.0$ keV data for XIS 1. We fitted all the spectra using XSPEC with a model comprising three plasma components, similar to previous studies: $apec1 + wabs^*(apec2 + pl)$. The APEC model assumes an emission from collisionally ionized diffuse gas. Here, (1) APEC is an unabsorbed thermal plasma with $kT = 0.1$ keV that mimics the local hot bubble (LHB), (2) $wabs^*apec2$ is the absorbed thermal plasma emitted from the SPS or LAS, and (3) $wabs^*pl$ is an absorbed power-law component representing the cosmic X-ray background (CXB). We assumed metal abundance $Z = Z_{\odot}$ for the LHB, whereas $Z = 0.2\,Z_{\odot}$ was assumed for the SPS and LAS, respectively (see Kataoka et al. 2013). For the CXB, we fixed the photon index $\Gamma = 1.41$, as determined by Kushino et al. (2002).

Table 2 lists the spectral fitting parameters for each analysis region, focusing particularly on the temperature $kT$ and emission measure (EM) of plasma component 2. We first fitted the data with the absorption column density ($N_{\rm H}$) as a free parameter, but the results were not constrained well owing to low photon statistics. Hence, we investigated the following two extreme cases: (1) $N_{\rm H}$ was fixed at the Galactic value provided by Dickey & Lockman (1990), and (2) $N_{\rm H}$ was fixed at zero. In each case, the resulting $kT$ value coincided within uncertainties. The reduced $\chi^2$ values for the fitting model were listed with the number of degrees of freedom. The left panel of Figure 4 shows the variations in $kT$ in $apec2$ along the Galactic longitude, whereas the right panel of Figure 4 shows the scatter plots of $kT$ and EM for each Galactic spur. The analysis results in the NPS region (open magenta circles) were from N1 to N6 of Kataoka et al. (2013). It was clear that the $kT$ of the SPS regions was
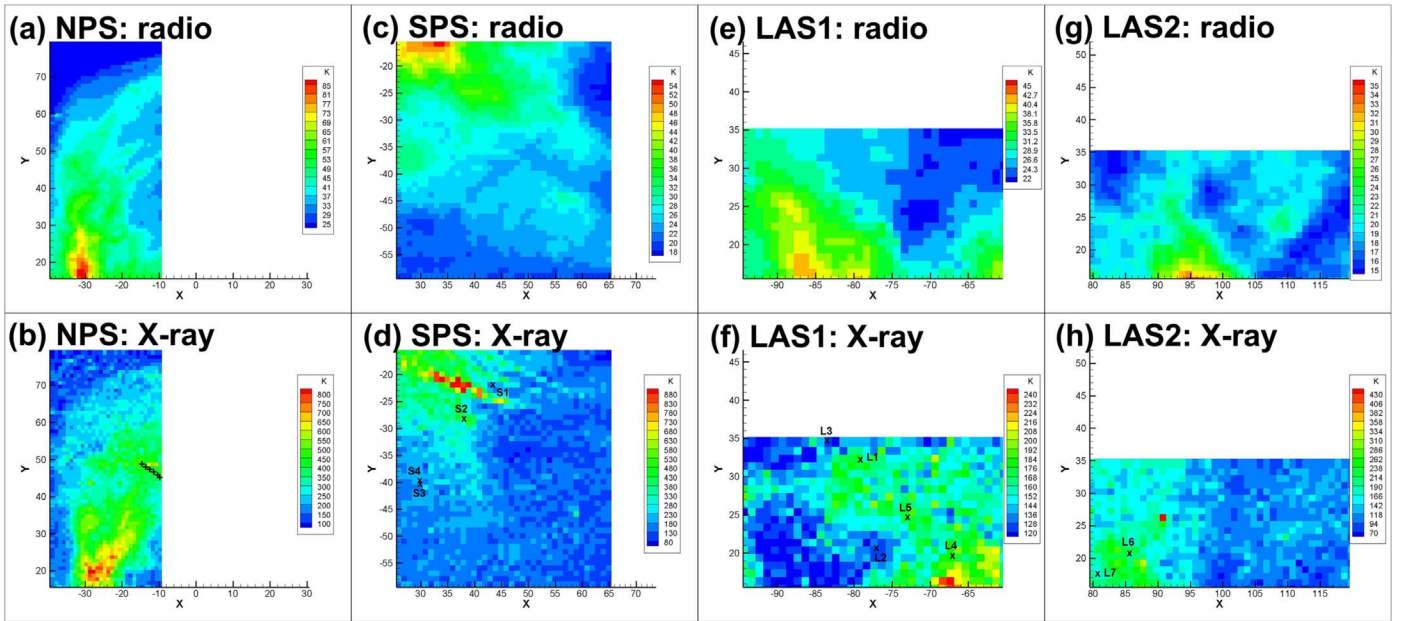
**Figure 2.** Close-up of Galactic spurs as observed from ROSAT (0.75 keV) and HASLAM (408 MHz) all-sky maps. (a) NPS: radio; (b) NPS: X-ray; (c) SPS: radio; (d) SPS: X-ray; (e) LAS1: radio; (f) LAS1: X-ray; (g) LAS2: radio; and (h) LAS2: X-ray. The X-ray map (ROSAT 0.75 keV) is shown in units of $10^{-6}$ counts s$^{-1}$ arcmin$^{-2}$. The radio map (Haslam 408 MHz) is shown in units of K. The cross indicates the pointing center of Suzaku observations analyzed herein (see Table 1). In panel (b), Suzaku pointing center for NPS (N1–6 of Kataoka et al. 2013) is shown as a plus sign.

generally $\simeq 0.3$ keV, which was higher than those in LAS1 and LAS2 concentrated around $\simeq 0.2$ keV, thereby suggesting different emission process origins.

## 3. Discussion

### 3.1. Difference of kT between NPS/SPS and LAS

In the previous section, we showed that the diffuse X-ray emission associated with the SPS and LAS was generally reproduced well by a thin plasma model assuming collisional ionized gas, but the temperature in the SPS was slightly higher than that in the LAS. Interestingly, the observed $kT \simeq 0.3$ keV in the SPS was consistent with those reported in the NPS/Loop I and Fermi bubble edges (Kataoka et al. 2018). These results suggested the same physical origin between the NPS and SPS, i.e., the shock heating of the Galactic halo gas through the significant Galactic explosion in the past. This idea was further supported by the recent eROSITA observations, which clearly exhibited X-ray bubbles with sharp edges, both north and south of the GC surrounding the Fermi bubbles, where the SPS was situated at the lowest edge of the south bubble (Predehl et al. 2020b).

By contrast, $kT \simeq 0.2$ keV observed in LAS1 and LAS2 was noteworthy because the temperature was typical of that generally observed in the Galactic halo gas (Yoshino et al. 2009; Nakashima et al. 2018), suggesting that the emissions were from local, unshocked halo gas. It was argued that each spiral arm rendered the local potential minimum on the order of 10% of the gravitational field of the Galaxy; hence, the interstellar gas will fall into the minimum with a typical velocity of $20-30$ [km s$^{-1}$] (Roberts 1969; Sofue 1973). It is noteworthy that the sound velocity of the interstellar gas is expressed as follows:

$$c_s = \sqrt{\gamma k_B T / \mu m_p} \simeq 15\left(\frac{T}{10^4 K}\right)^{1/2} \text{km s}^{-1}, \qquad (2)$$

where $\mu \simeq 0.61$ is the mean molecular weight and $T \sim 10^4$ [K] is the temperature of the interstellar gas. Hence, the falling gas causes a strong shock of $M \sim 2-3$, where $M$ is the Mach number, resulting in a significant increase in the star formation rate because the compression of the gas density scales as $n \propto M^2$. Moreover, if the Galactic shock is isothermal and the magnetic field $B$ is parallel to the arm, $B \propto M^2$, then the radio emissivity scales as $\propto nB^2 \propto M^6$. Therefore, the local arms will be sufficiently bright in the radio map, as first confirmed by Mills (1959).

Meanwhile, the X-ray-emitting gas had a sound velocity of $c_s \sim 200$ km s$^{-1}$ for $kT \simeq 0.2$ keV; hence, it remained unshocked. Even in such a high-velocity gas, an increasing density reflecting the local gravitational potential may occur, although detailed simulations/observations are necessary. Such a gentle pileup of X-ray-emitting gas may account for the observed enhancement around the LAS. Because the EM of thin thermal X-ray gas scales as EM $\propto n^2$, only a 20%–30% increase in X-ray gas density, $n$, is required to enhance the X-ray gas, whose temperature is $kT \simeq 0.2$ keV, as indicated from the observation.

### 3.2. Thickness and Offset of NPS/SPS

We observed a significant offset between the radio and X-ray intensity distributions not only in the NPS but also in the SPS and LAS structures, although their origins are likely to be different, as indicated in the previous section. For the NPS/SPS, the situation can be interpreted based on the diffusive shock process. The relativistic electrons accelerated via the forward shock (FS) emit synchrotron radiation in the radio band, whereas swept-up, compressed gas emitted thin thermal X-ray radiation in the reverse-shock (RS) region. In this context, the observed offset between radio and X-rays might be related to the thickness and positional offset of the FS/RS regions. In fact, X-ray-emitting shells are typically observed on
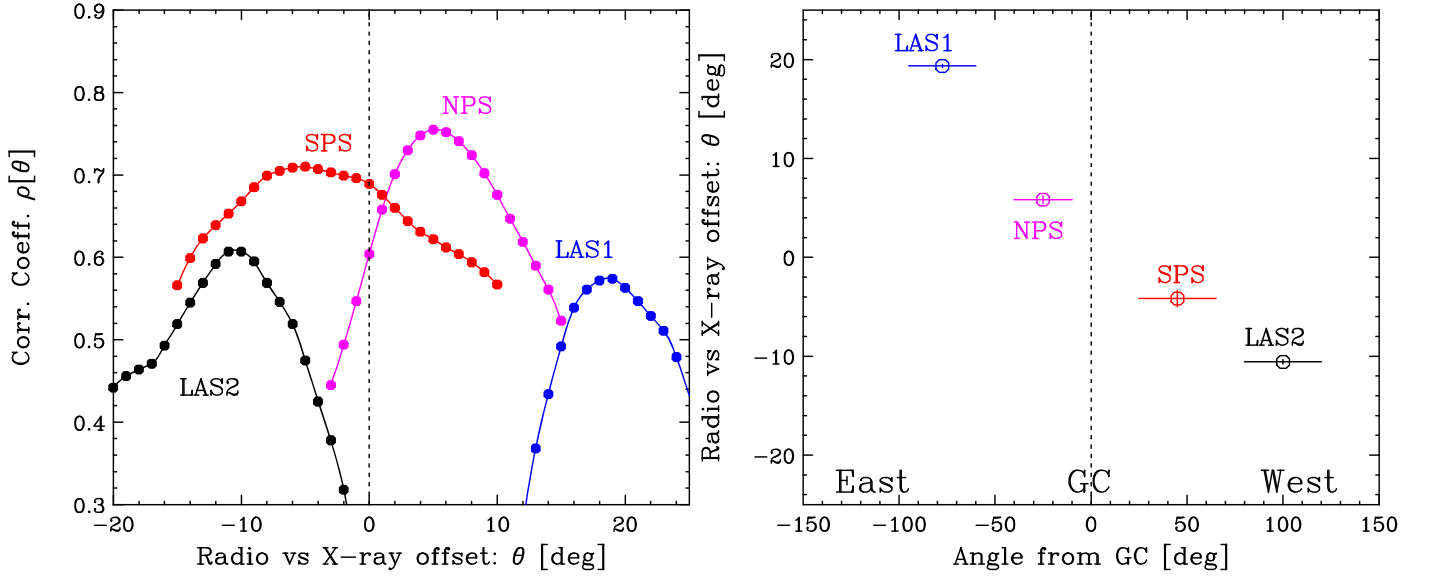
**Figure 3.** Left: correlation coefficient calculated between radio (408 MHz) and X-ray (0.75 keV) spurs, as defined in Figure 2. The angle in horizontal axis becomes positive when X-ray structure is offset toward GC for spurs in Galactic east, whereas it becomes negative for spurs in the west. Right: positional offset of each Galactic spur plotted against Galactic longitude. In all cases, X-ray spurs are located on the inner side of corresponding radio spurs.

the inner side of the radio shell in the case of SNRs (e.g., Gaetz et al. 2000 for the case of E0102-72.3).

From Kataoka et al. (2015) we adopt a simple model in which two spherical bubbles that mimic the north and south are embedded in the center of a gaseous halo. The radius of the outer shell corresponding to the NPS/SPS is $R \simeq 5$ kpc, and the shock velocity is $v_{\rm sh} \simeq 300$ km s$^{-1}$, as indicated by X-ray observations. First, the dynamical timescale $t_{\rm dyn}$ in which the bubble expands to radius $R$ is expressed as $t_{\rm dyn} \simeq R/v_{\rm sh}$. For example, $t_{\rm dyn}$ is 16 Myr in case of $R = 5$ kpc and $v_{\rm sh} = 300$ km s$^{-1}$.

The thickness of the FS region can be approximated as follows:

$$d_{\rm FS} \simeq \left( \frac{k_1}{u_1} + \frac{k_2}{u_2} \right) \simeq \frac{5}{v_s} \frac{\xi r_g c}{3}, \tag{3}$$

where $k_1$ and $k_2$ are the diffusion coefficients; $u_1$ and $u_2$ are the plasma velocities in the upstream/downstream of the FS, respectively; $v_s$ is the shock velocity; $r_g$ is the gyro radius; and $\xi$ ($>1$) is a constant factor (Drury 1983). Furthermore, we assume that the diffusion coefficient $k_1 = k_2 \simeq \xi \ r_g c/3$. In addition, $v_s = u_1 = 4u_2$, $r_g = \gamma {\rm m}_{ec}^2/eB$, where $\gamma$ is the Lorentz factor of the accelerated electrons. The acceleration timescale of electrons with energy $\gamma {\rm m}_{ec}^2$ is expressed as

$$t_{\rm acc} = \frac{20 \xi r_g c}{3 u_1^2} = \frac{4 d_{\rm FS}}{v_{\rm sh}}. \tag{4}$$

For comparison, the radiative cooling time of electrons emitting 408 MHz of radio emission is expressed as

$$t_{\rm cool,R} = \frac{3 m_e c}{4 \sigma_T U_B \gamma} \simeq 20 \left( \frac{B}{15 \ \mu{\rm G}} \right)^{-3/2} {\rm Myr}, \tag{5}$$

where $m_e$ is the rest mass of electrons, $\sigma_T = 6.65 \times 10^{-25}$ cm$^{-2}$ is the Thomson cross section, and $U_B$ is the magnetic field density. We assume that the shock compression ratio of the magnetic field is $\simeq 4$. Hence, the cooling time is slightly longer

but almost comparable to $t_{\rm dyn}$. Therefore, the thickness of the radio shell, $d_R$, is approximated by equating $t_{\rm acc}$ and $t_{\rm dyn} \simeq t_{\rm cool,R}$, resulting in $d_R \simeq d_{\rm FS} \simeq 1/4 \ R$. This is on the order of 1 kpc, which is consistent with the observed thickness of the radio emission region of the NPS/SPS.

Next, we consider the dynamics of the X-ray shell. First, the radiative cooling timescale of the X-ray-emitting gas can be expressed as

$$t_{\rm cool,X} \simeq \frac{1.1 \times 10^5 \ T_6^{1.7}}{n \ {\rm cm}^{-3}} \ {\rm yr} \ {\rm for} \ 10^5 \ {\rm K} \ < T < 10^{7.3} \ {\rm K}, \tag{6}$$

where $n$ is the number density of the X-ray-emitting gas and $T_6$ is the temperature in units of $10^6$ K (Equation (34.4) of Draine 2011). We further modified the above equation assuming subsolar metallicity $Z \simeq 0.2 \ Z_\odot$ (Kataoka et al. 2013), which leads to

$$t_{cool,X} \simeq 50 \left( \frac{v_{sh}}{300 \ {\rm km \ s}^{-1}} \right)^{3.4} \left( \frac{n}{0.01 \ {\rm cm}^3} \right)^{-1} {\rm Myr} \tag{7}$$

(see also Inoue et al. 2017). We assume that the X-ray-emitting gas does not cool during the expansion time, $t_{\rm dyn}$; hence, the thickness of the X-ray shell is determined by the amount of halo gas piled up in the RS region to form the NPS.

As the underlying halo gas density profile, we assume a hydrostatic isothermal model expressed as

$$n(r) = n_0 \left[ 1 + \left( \frac{r}{r_c} \right)^2 \right]^{-1}, \tag{8}$$

where $n(r)$ is the gas density [cm$^{-3}$] at radius $r$ from the GC; $n_0$ is the density at $r = 0$; and $r_c$ is the core radius, which we set as $r_c = 0.5$ kpc from the observation (Kataoka et al. 2015). The thickness of the X-ray shell, $d_X$, can be determined from the conservation of the swept gas mass as follows:

$$\int_0^R 4\pi r^2 n(r) dr = 4\pi R^2 [4n(R)] d_X, \tag{9}$$

**Table 2**
Suzaku Observations and Analysis Results

| SrcID | ObsID[a] | R.A.[b] (deg) | Decl.[b] (deg) | $l$[b] (deg) | $b$[b] (deg) | Exposure[c] (ks) | $N_H/N_{H,Gal}$[d] | $kT$[e] (keV) | EM[f] ($\times 10^{-2}$ cm$^{-6}$ pc) | $\chi^2$/ dof[g] |
|---|---|---|---|---|---|---|---|---|---|---|
| | | | | | South Polar Spur | | | | | |
| S1 | 705013010 | 265.961 | −76.342 | 317.082 | −22.458 | 42.4 | <0.61 | $0.277^{+0.029}_{-0.023}$ | $0.62^{+0.14}_{-0.12}$ | 234.0/231 |
| S2 | 701052010 | 292.839 | −72.655 | 322.501 | −28.769 | 113.5 | 7.0−10.8 | $0.301^{+0.004}_{-0.003}$ | $4.19 \pm 0.10$ | 602.2/418 |
| S3 | 806082010 | 321.058 | −63.430 | 330.620 | −40.844 | 36.3 | 2.3−2.8 | $0.272^{+0.013}_{-0.020}$ | $2.09^{+0.42}_{-0.22}$ | 210.9/160 |
| S4 | 806079010 | 319.721 | −63.575 | 330.734 | −40.236 | 69.5 | 1.0−5.0 | $0.292^{+0.011}_{-0.010}$ | $1.81 \pm 0.14$ | 444.1/312 |
| | | | | | Local Arm Spur 1 | | | | | |
| L1 | 704008010 | 265.005 | 52.168 | 79.523 | 31.837 | 22.5 | 2.4−6.7 | $0.196^{+0.025}_{-0.014}$ | $2.77^{+0.97}_{-1.03}$ | 111.2/90 |
| L2 | 403008010 | 282.080 | 47.990 | 77.411 | 20.299 | 44.4 | <1.4 | $0.204^{+0.029}_{-0.020}$ | $1.20^{+0.61}_{-0.40}$ | 299.4/256 |
| L3 | 704051010 | 260.921 | 55.895 | 83.893 | 34.333 | 35.9 | 5.8−14.8 | $0.217 \pm 0.042$ | $0.60^{+0.77}_{-0.24}$ | 139.9/166 |
| L4 | 100017010 | 279.235 | 38.784 | 67.448 | 19.237 | 11.4 | <2.6 | $0.229^{+0.014}_{-0.011}$ | $1.83 \pm 0.27$ | 147.2/104 |
| L5 | 707038010 | 274.923 | 45.536 | 73.363 | 24.300 | 30.9 | <1.3 | $0.266^{+0.018}_{-0.023}$ | $1.52^{+0.39}_{-0.22}$ | 183.3/168 |
| | | | | | Local Arm Spur 2 | | | | | |
| L6 | 807071010 | 160.083 | −35.328 | 274.839 | 20.293 | 45.7 | <1.0 | $0.229^{+0.008}_{-0.007}$ | $3.66 \pm 0.35$ | 304.7/258 |
| L7 | 808063010 | 163.275 | −40.329 | 279.735 | 17.153 | 152.2 | 3.3−4.4 | $0.197^{+0.011}_{-0.008}$ | $2.97 \pm 0.51$ | 801.3/585 |

**Notes.**
[a] Suzaku observation ID.
[b] R.A., decl., Galactic longitude, Galactic latitude of Suzaku observations.
[c] Suzaku XIS exposure in ks.
[d] The ratio of absorbing column density to the full Galactic column along the line of sight when $N_H$ was left free in the spectral fitting.
[e] Temperature of the Galactic halo gas fitted with the APEC model for the fixed abundance $Z = 0.2\ Z_\odot$.
[f] Emission measure of the Galactic halo gas fitted with the APEC model for the fixed abundance $Z = 0.2\ Z_\odot$.
[g] $\chi^2$ of the spectral fitting to the model APEC1+WABS*(APEC2+PL), where we fixed $kT$ at 0.1 keV and assumed a solar abundance, $Z_\odot$, for APEC1. A photon index of PL representing the cosmic X-ray background (CXB) is 1.41 (Kushino et al. 2002). Since WABS is not well constrained owing to low photon statistics, we fixed them to zero for the values listed here.

where $4n(R)$ is the density of the shocked halo gas in the downstream, assuming the strong shock of a specific heat ratio of 5/3. Using Equation (8), we obtained $d_X \sim 1/4\, R \sim 1.3$ kpc for $R = 5$ kpc. This is consistent with the observed thickness of the NPS/SPS, as shown in the X-ray map, and explains the approximate similarity between the radio/X-ray thicknesses, $d_R \sim d_X$. Hence, the observed offset of $\sim 5°$, which corresponds to 0.7 kpc between the radio and X-ray NPS, may indicate that the FS is located outside the RS by 0.7 kpc on average; however, approximately half of the FS/RS regions may have been overlapped. This is because the radio emission becomes maximum around the forefront of the FS owing to compressed magnetic field via the synchrotron emission, whereas the X-ray emission would have a broad maximum in the RS reflecting a density gradient of the swept-up halo gas.

### 3.3. Origin of Radio/X-Ray Offset in LAS

As reviewed in Section 1, the radio emissions associated with the LASs have been well known since the 1950s; however, the origin of radio spurs in the tangential direction of the Local Arm is yet to be elucidated. Sofue (1973, 1976) suggested that spurs immediately above the Galactic shock may be generated by the inflation of magnetic fields through the Parker instability triggered by the Galactic shock wave. Such an inflation is promoted by the strong compression of the gas and magnetic fields; subsequently, the magnetic force lines above the shock lane will be stretched into the halo perpendicular to the Galactic plane. This is consistent with

measurements of vertically extended magnetic fields, as inferred from polarized far-infrared dust emissions in the Local Arm directions (Mathewson & Ford 1970; Planck Collaboration et al. 2015).

In such a scenario, the formation of radio spurs may be substantially delayed after the Galactic shocks are being activated. First, shock-compressed interstellar gas (mostly H I and H$_2$) increases the magnetic field strength along the arm and increases the rate of star formation at the shock front. Thus, the regions of the newly born stars (or H II regions) lie just outside the shock front. The typical timescale for the evolution of massive stars is $t_{SF} \sim 10^6$-$10^7$ yr; thus, the H II region *lags behind* the shock by $\simeq t_{SF} \times (v_{rot} - v_\Omega) \simeq 1$ kpc along the direction of Galactic rotation, where $v_{rot} \simeq 220$ km s$^{-1}$ is the rotation speed of the Galaxy and $v_\Omega \sim 100$–150 km s$^{-1}$ is the pattern speed of the spiral density wave. Accordingly, offset by $\sim 1$ kpc $\times \sin(p) \sim 100$ pc is anticipated in the direction perpendicular to the Galactic arm for a pitch angle of $p \sim 12°$. When the stars end their lives, supernovae happen to accelerate cosmic-ray electrons, which may take $10^4$–$10^5$ yr further. Then, accelerated electrons propagate into the nonthermal bank perpendicular to the disk along the arm within a timescale of $h/v_A \simeq \sim 10^6$ yr, where $h \simeq 100$ pc is the height of the nonthermal bank and $v_A \simeq 10$–100 km s$^{-1}$ is the Alfvén velocity.

In this context, we can qualitatively interpret the offset between radio and X-rays in the LAS as follows. The position of the radio spur may include an offset compared with the Galactic shock position because we expect $\sim 10^6$–$10^7$ yr of delay for their formation. Radio spurs originate in synchrotron
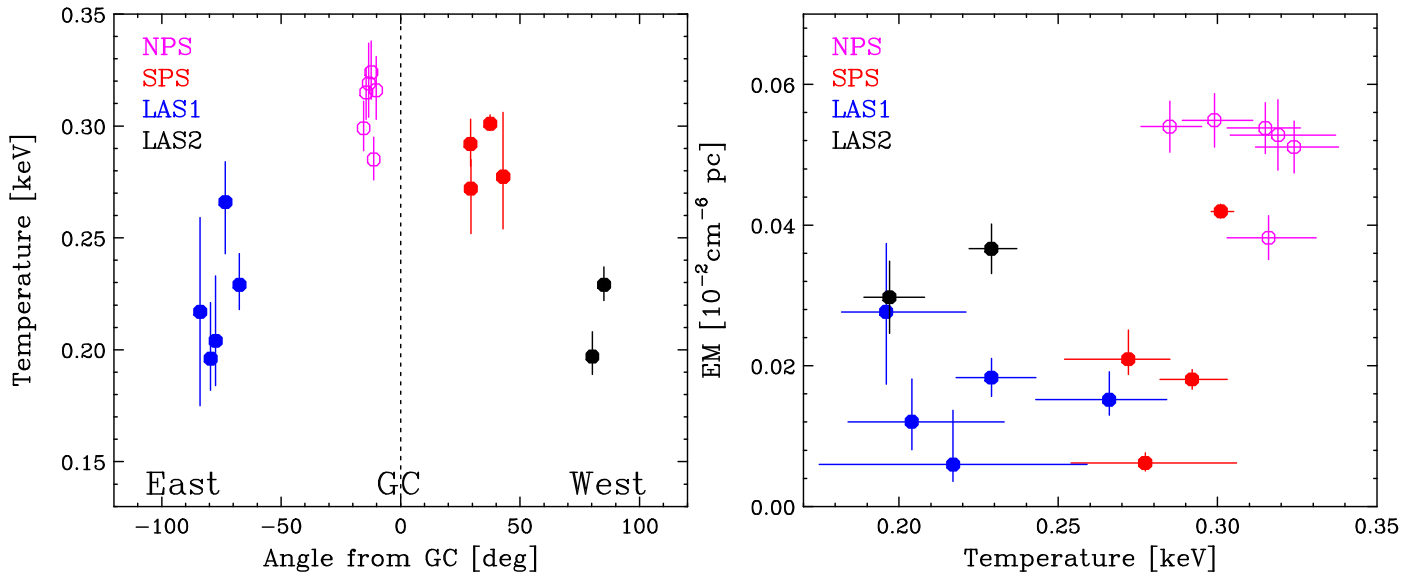
**Figure 4.** Left: temperature ($kT$ of APEC2 in Table 2) variation in halo gas along Galactic plane. Right: scatter plot of temperature vs. EM of halo gas ($kT$ and EM of APEC2 in Table 1). Analysis results in the NPS region were from N1 to N6 of Kataoka et al. (2013).

emission by cosmic-ray electrons, which are likely generated by SNRs. Hence, time delays due to stellar evolution, particle acceleration, and diffusion should occur. By contrast, the LAS diffuse X-ray emission may be associated with the Galactic shock region if the Galactic halo gas is trapped by the local potential minimum of the spiral arm. Such an association is often observed in nearby galaxies (Tyler et al. 2004; Long et al. 2014). In such cases, the X-ray emission from the LAS is expected to *lead* the radio emission by ~a few × $10^6$ yr. Assuming a typical distance of ≃1 kpc to the regions of the Orion–Cygnus arm, which primarily contributes to the radio/X-ray emissions of the LAS, the observed 10°–20° offset corresponds to ~100 pc, which is approximately consistent with the horizontal size (~30° from Figure 1) of the radio bank in the all-sky map, where we assumed ~100 pc.

### 3.4. Further Comments on the NPS

Finally, we revisit some aspects related to the distance and possible origin of the NPS. As noted in Section 1, the NPS was initially thought to be the remnants of an old supernova close to the Sun rather than a distant structure associated with the GC activity. Although this idea is not well supported by a number of recent X-ray and gamma-ray observations, it was recently claimed that the NPS distance between 70 and 135 pc depends on the galactic latitudes, according to near-infrared and optical photometry and Gaia DR2 (Das et al. 2020). However, note that Das et al. (2020) observed the extinction of stars toward the NPS; thus, they measured the distance to the cold dust (typical temperature $T \simeq 10^3$ K) rather than the X-ray brightness of the NPS itself ($T \simeq 10^6$–$10^7$ K). In fact, such foreground dust absorption in the Aquila Rift is generally used to provide a lower limit on the distance to the NPS (e.g., Sofue 1994; Snowden et al. 1995; Lallement et al. 2016), but it is unlikely that cold dust and the hot X-ray plasma of the NPS coexist. Similarly, a wide range of the distance depending on the position in the NPS, as proposed by Das et al. (2020), is also unlikely if the NPS is a single continuous structure.

However, let us consider the situation if the NPS is really a structure close to the Sun, in the context of observed thickness

and offset, as discussed in Section 3.2. Now, the radius of the NPS is as small as $R \simeq 100$ pc, and the width of the FS, $d_{FS}$, is $\simeq 1/4~R$, as anticipated from $t_{dyn} \simeq t_{acc} \simeq 0.3$ Myr (see Equations (4) and (5)). Assuming a typical magnetic field strength of $B \simeq 10~\mu$G for an old SNR (e.g., Loru et al. 2020), the cooling time of electrons, $t_{cool,R}$, is much longer than $t_{acc}$; thus, the accelerated electrons remain uncooled, and the radio-bright NPS would be more spherical in shape rather than forming a sharp shell. In contrast, the X-ray shell is formed as previously mentioned, i.e., by sweeping up the interstellar medium. We would expect quite different morphologies for the radio (sphere-like) and X-ray (shell), which are far from the observation. This is an indirect but additional reason supporting why we think that the NPS is a giant structure associated with the GC.

Finally, note that the most recent observation by HaloSAT enabled coverage of the entire bright NPS through 14 observations of approximately 30 ks each (LaRocca et al. 2020). These observations provide the first complete survey of the NPS thanks to a wide FOV. While the observed X-ray spectrum is well fitted by two thermal components of $kT_{cool} \simeq 0.1$ keV and $kT_{hot} \simeq 0.3$ keV, there is a gradient of temperature across the NPS such that the inner arc temperature is slightly warmer ($kT_{hot} \simeq 0.31$ keV) than the outer arc ($kT_{hot} \simeq 0.26$ keV). For comparison, the NPS results presented in Figure 4 ($kT = 0.30 \pm 0.01$ keV) were extracted from Kataoka et al. (2013), in which all Suzaku pointings were arranged in the inner arc of the NPS. Moreover, LaRocca et al. (2020) provided a new indication that the cool component also belongs to the NPS rather than to local hot bubbles (LHB). Similarly, even the modeled hot component of $kT \simeq 0.30$ keV further complicated the analysis by adding a halo gas emission of $kT \simeq 0.2$ keV in addition to the NPS (e.g., Gu et al. 2016; Miller & Bregman 2016). Although the same conclusion is always reached, i.e., the NPS is a distant object in the kiloparsec range, future deep observations by wide-field satellites such as HaloSAT and eROSITA will provide a new insight to resolve such complexity in the modeling of NPS spectra.

## 4. Conclusion

Herein we analyzed two types of Galactic spurs observed from both radio and X-rays, i.e., the NPS and SPS. These spurs are likely to be the remnants of Galactic explosions in the past and are hence located near the GC, whereas LASs are associated with local spiral arms. The important results of this study are as follows:

1. The X-ray emission from the NPS and SPS was well represented by a thin thermal plasma of $kT \simeq 0.3\,\mathrm{keV}$; hence, shock-heated halo gas was most likely the origin.
2. The other X-ray emissions from the LAS were represented by a thin thermal plasma of $kT \simeq 0.2\,\mathrm{keV}$. This can be regarded as the weak condensation of halo gas in the arm potential or star formation activity without shock heating.
3. The positional offsets observed from the NPS and SPS in the radio and X-ray maps were $\simeq 5°$, where the X-ray emissions were from the inner side of the radio shell. A similar width of radio/X-ray structures and positional offsets are naturally interpreted if the radio emission is primarily from the FS front, whereas the X-rays were from the downstream of the RS. The thickness of each shock was $\sim 1.3\,\mathrm{kpc}$, half of which was superposed onto each other.
4. The positional offset of $10°$–$20°$ was observed in the LAS; however, it might be attributed to different origins. Radio spurs might possibly be associated with the nonthermal bank, which might have an offset of $\sim 100$ pc compared with the Galactic shock position. By contrast, the X-ray spurs might be closer to the Galactic shock if the halo gas was simply trapped by the Local Arm potential or related to the star formation activity in the spiral arm.

We are cognizant that there exist more structures that are possibly related to various Galactic spurs and even to Fermi bubbles' edges, which are marginally visible but not conclusive based on the current HASLAM and ROSAT data sets. Moreover, a correlation analysis for the entire Loop I structure is expected to be conducted, but it is still limited to the brightest eastern part known as the NPS. All-sky observations with unprecedented sensitivity and resolution, for example, Planck and eROSITA at different energies, will provide further opportunities to confirm the physical origin and structure of Galactic spurs in the near future.

## ORCID iDs

Jun Kataoka ● https://orcid.org/0000-0003-2819-6415
Yoshiaki Sofue ● https://orcid.org/0000-0002-4268-6499
Yoshiyuki Inoue ● https://orcid.org/0000-0002-7272-1136

## References

Berkhuijsen, E. M., Haslam, C. G. T., & Salter, C. J. 1971, A&A, 14, 252
Das, K. K., Zucker, C., Speagle, J. S., et al. 2020, MNRAS, 498, 5863
Dickey, J. M., & Lockman, F. J. 1990, ARA&A, 28, 215
Dobler, G., & Finkbeiner, D. P. 2008, ApJ, 680, 1222
Draine, B. T. 2011, Physics of the Interstellar and Intergalactic Medium (Princeton, NJ: Princeton Univ. Press)
Drury, L. Oc. 1983, RPPh, 46, 973
Fujimoto, M. 1968, in IAU Symp. 29, Non-stable Phenomena in Galaxies (Yerevan: NAS RA), 453
Gaetz, T. J., Butt, Yousaf, M., et al. 2000, ApJ, 534, L47
Gu, L., Mao, L., Constantini, E., & Kaastra, J. 2016, A&A, 594, A78
Haslam, C. G. T., Salter, C. J., Stoffel, H., & Wilson, W. E. 1982, A&AS, 47, 1
Henley, D. B., & Shelton, R. L. 2013, ApJ, 773, 92
Henley, D. B., Shelton, R. L., Kwak, K., Joung, M. R., & Mac Low, M.-M. 2010, ApJ, 723, 935
Inoue, Y., Lee, S.-H., Tanaka, Y., & Kobayashi, S. 2017, APh, 90, 14
Ishisaki, Y., Maeda, Y., Fujimoto, R., et al. 2007, PASJ, 59, 113
Kataoka, J., Sofue, Y., Inoue, Y., et al. 2018, Galax, 6, 27
Kataoka, J., Tahara, M., Totani, T., et al. 2013, ApJ, 779, 57
Kataoka, J., Tahara, M., Totani, T., et al. 2015, ApJ, 807, 77
Kushino, A., Ishisaki, Y., Morita, U., et al. 2002, PASJ, 54, 327
Lallement, R., Snowden, S., Kuntz, K. D., et al. 2016, A&A, 595, A131
LaRocca, D. M., Kaaret, P., Kuntz, K. D., et al. 2020, ApJL, 904, 54L
Long, K. S., Kuntz, K. D., Blair, W. P., et al. 2014, ApJS, 212, 21
Loru, S., Pellizoni, A., Egro, E., et al. 2020, MNRAS, 500, 5177
Mathewson, D. S., & Ford, V. L. 1970, MmRAS, 74, 139
Miller, M. J., & Bregman, J. N. 2016, ApJ, 829, 9
Mills, B. Y. , 1959, PASP, 71, 267
Nakanishi, H., & Sofue, Y. 2006, PASJ, 58, 847
Nakashima, S., Inoue, Y., Yamasaki, N., et al. 2018, ApJ, 862, 34
Parker, E. N. 1966, ApJ, 145, 811
Parker, E. N. 1969, SSRv, 9, 651
Planck Collaboration, Ade, P. A. R., Aghanim, N., et al. 2013, A&A, 554, A139
Planck Collaboration, Ade, P. A. R., Aghanim, N., et al. 2015, A&A, 576, A104
Predehl, P., Andritschke, R., Arefiev, V., et al. 2020a, A&A, in press (arXiv:2010.03477)
Predehl, P., Sunyaev, R. A., Becker, W., et al. 2020b, Natur, 588, 227
Roberts, W. W. 1969, ApJ, 158, 123
Snowden, S. L., Freyberg, M. J., Plucinsky, P. P., et al. 1995, ApJ, 454, 643
Sofue, Y. 1973, PASJ, 25, 207
Sofue, Y. 1976, A&A, 48, 1
Sofue, Y. 1977, A&A, 60, 327
Sofue, Y. 1994, ApJ, 431, L91
Sofue, Y. 2000, ApJ, 540, 224
Sofue, Y. 2015, MNRAS, 447, 3824
Su, M., Slatyer, T. R., & Finkbeiner, D. P. 2010, ApJ, 724, 1044
The Astropy Collaboration, Price-Whelan, A. M., Sipöcz, B. M., Günther, H. M., et al. 2018, AJ, 156, 123
The Astropy Collaboration, Robitaille, T., Tollerud, E. J., Greenfield, P., et al. 2013, A&A, 558, A33
Tyler, K., Quillen, A. C., LaPage, A., & Rieke, G. H. 2004, ApJ, 610, 213
Yoshino, T., Mitsuda, K., Yamasaki, N. Y., et al. 2009, PASJ, 61, 805